ACS APPLIED MATERIALS & INTERFACES

Research Article

www.acsami.org

Yolk–Shell Nanostructured Fe_3O_4@$NiSiO_3$ for Selective Affinity and Magnetic Separation of His-Tagged Proteins

Yang Wang,[†] Guangchuan Wang,[‡] Yun Xiao,[†] Yuling Yang,[†] and Ruikang Tang*[,†,‡]

[†]Center for Biomaterials and Biopathways, Department of Chemistry, Zhejiang University, Hangzhou, Zhejiang 310027, China

[‡]Qiushi Academy for Advanced Studies, Zhejiang University, Hangzhou, China

Supporting Information

ABSTRACT: Recent developments of nanotechnology encourage novel materials for facile separations and purifications of recombinant proteins, which are of great importance in disease diagnoses and treatments. We find that Fe_3O_4@$NiSiO_3$ with yolk–shell nanostructure can be used to specifically purify histidine-tagged (His-tagged) proteins from mixtures of lysed cells with a recyclable process. Each individual nanoparticle composes by a mesoporous nickel silicate shell and a magnetic Fe_3O_4 core in the hollow inner, which is featured by its great loading efficiency and rapid response toward magnetic fields. The abundant Ni^{2+} cations on the shell provide docking sites for selective coordination of histidine and the reversible release is induced by excess imidazole solution. Because of the Fe_3O_4 cores, the separation, concentration, and recycling of the nanocomposites become feasible under the controls of magnets. These characteristics would be highly beneficial in nanoparticle-based biomedical applications for targeted-drug delivery and biosensors.

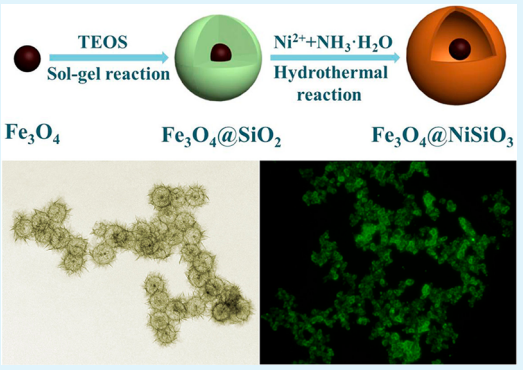

KEYWORDS: *magnetic nanocomposites, yolk–shell, protein separation, recyclability*

INTRODUCTION

Core–shell nanoparticle architectures have received considerable attention because of the advantages of structural and functional combinations.[1−4] Their physical and chemical properties can be tuned by controlling chemical compositions and relative sizes of cores and shells.[5−7] In recent years, yolk–shell structures or so-called "nanorattles" represent a new class of special core–shell structures with interior core, void space, and permeable outer shell. They are always featured by the unique properties such as low density, large surface area, high permeability, multifunctionality, and excellent loading capacity.[8−14] Specifically, such yolk–shell structures composed of magnetic cores and functional shells endue nanocomposites possible applications in magnetic-targeted drug delivery, recycling of nanocatalyst, selective separation of target molecules and magnetically controllable on–off reactions.[15−18]

With the coming of the post genome era, proteomics has been developed and be widely used for disease diagnosis and treatment. However, it is important to easily separate and rapidly manipulate the recombinant proteins during the process of proteomics research. Currently, immobilized metal ion affinity chromatography (IMAC) has been considered as one of the most effective approaches for the separation and enrichment of biomolecules among the developed of many methodologies, which achieves the reversible association and dissociation of His-tagged proteins by nickel(II) ions. However, this technique has limitations including the need for pretreatment to remove the cell debris and colloid contaminants, high pressure drop, and long separation time as well as difficult manipulations.[19−21] In order to circumvent these limitations, new separation systems based on magnetic nanomaterials have recently been reported (e.g., nitrilotriacetic acid,[22−24] Au–Ni–Au triblock nanorods,[25] core–shell structured of Ni/NiO nanoparticles,[26] and Fe_2O_3/SiO_2@NiO microspheres[27,28]). Unfortunately, weak magnetic properties and poor recyclability still appear in these new separation systems, which restrict the practical applications.

Silicates have attracted significant interest due to their rich porous structures, good thermal and chemical stability, tunable composition, low-cost and abundant supply, and have wide applications in catalyst support, molecular sieve, gas adsorption, wastewater treatment, and biomolecule separation, etc.[29−35] In particular, nickel silicate has high Ni^{2+} density, which can be directly applied for purifying His-tagged proteins.[36−38] Herein, in this work, we report a facile and effective route for synthesis of yolk–shell structured Fe_3O_4@$NiSiO_3$ magnetic nanocomposites (Scheme 1). Each Fe_3O_4@$NiSiO_3$ nanocomposite has a magnetic iron oxide core and a mesopores and hollow nickel silicate shell with high specific surface area, which can provide high densities of Ni^{2+} and responses toward external magnetic fields, which will be applied for selective binding and magnetic separation of His-tagged proteins from protein mixture.

Received: July 31, 2014
Accepted: October 10, 2014
Published: October 10, 2014

Scheme 1. Schematic Illustration of Synthesis of Yolk–Shell Structured Fe_3O_4@$NiSiO_3$ Magnetic Nanocomposites

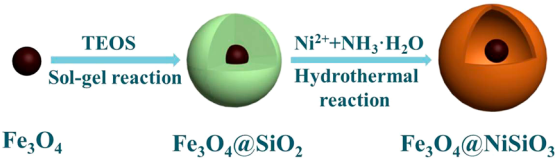

To the best of our knowledge, this is a first report about a facile route for synthesis of Fe_3O_4@$NiSiO_3$ yolk–shell nanostructure with efficiently selective affinity and magnetic separation of His-tagged proteins.

EXPERIMENTAL SECTION

Chemicals. 1-Octadecene, $NH_3{\cdot}H_2O$ (25%–28%), TEOS, NaOH, $FeCl_3{\cdot}6H_2O$, $NiCl_2{\cdot}6H_2O$, oleic acid, ammonia chloride, and cetyltrimethylammonium bromide (CTAB) were bought from Aladdin Chemical Reagent Co. Ltd. China. All chemical agents were of analytical grade and used directly without further purification.

Synthesis of Fe_3O_4 Nanoparticles. Fe_3O_4 NPs were prepared according to the previous reported.[39] First, 2.7 g $FeCl_3{\cdot}6H_2O$ was dissolved in 30 mL of water, and then a mixture solution of ethanol (40 mL), hexane (70 mL), and oleic acid (9.5 mL) was added and magnetically stirred vigorously for 30 min. Subsequently, 0.24 g NaOH was added and magnetically stirred and reflux for 4 h at 70 °C. When the reaction was completed, the organic layer containing $Fe(oleate)_3$ complex was obtained by using a separatory funnel separated from the resultant solution. The solid was washed with water and dried at 80 °C overnight. For synthesis of monodisperse magnetite nanocrystals, $Fe(oleate)_3$ was dispersed in a mixed solution contained oleic acid (9.6 mL) and 1-octadecene (62.5 mL) at room temperature and degassed with N_2 for 30 min. Then, the mixture was heated to 290 °C with a rate of 5 °C min^{-1} under N_2 flow and further heated to 320 °C for 1 h. When the reaction was completed, the resulting solution with black color was cooled to room temperature, and was precipitated by adding 500 mL acetone and centrifuged at 15 000 rpm for 15 min. Then the Fe_3O_4 nanoparticles were redispersed in chloroform. The purification process was repeated for three times and after that, Fe_3O_4 nanoparticles were dispersed in chloroform for further applications.

Synthesis of Fe_3O_4@SiO_2 Core–Shell Nanoparticles. Fe_3O_4 nanoparticles in chloroform (0.5 mL, 40 mg/mL) were poured into a CTAB solution (5 mL, 55 mM) and the resulting solution was stirred vigorously for 30 min. The formation of an oil-in-water microemulsion resulted in a turbid brown solution. The resulting solution was heated up to 60 °C and aged for 30 min to evaporate chloroform, and the resulting turbid brown solution was turned to transparent black Fe_3O_4/CTAB solution. The resulting solution was added to a mixture of water (45 mL) and NaOH solution (0.3 mL, 0.2 M) and then heated to 70 °C. 0.6 mL of TEOS was added and the solution was stirred for 3 h. After washing by ethanol and water, the obtained Fe_3O_4@SiO_2 core–shell nanoparticles were dispersed in 20 mL of ethanol for further applications.

Synthesis of Fe_3O_4@$NiSiO_3$ Yolk–Shell Nanocomposites. The above-prepared Fe_3O_4@SiO_2 solution was underwent ultrasonication for 30 min. $NiCl_2{\cdot}6H_2O$ (133.3 mg) and NH_4Cl (276.5 mg) were dissolved in a mixture solution containing deionized water (10 mL), ethanol (10 mL), and ammonia solution (1 mL, 28%). These two solutions were mixed with each other and transferred into a Teflon-lined stainless-steel autoclave (50 mL) and sealed to heat at 160 °C for 12 h. After the reaction, the autoclave was cooled to the room temperature. The aurantius precipitate was collected by centrifugation and washed with deionized water and ethanol in sequence, and then dried in a vacuum at 40 °C overnight.

Selective Binding and Separation of His-Tagged GFP. The PBS solutions of His-tagged green-fluorescent protein (GFP) or normal GFP proteins (250 μg/mL) were prepared. Fe_3O_4@$NiSiO_3$ nanocomposites (1 mg) were added into the above PBS solution (1 mL) and incubated with shaking for 30 min at room temperature. Subsequently, the precipitates were separated from the mixture solution by using an external field. Then, the precipitates were added to an imidazole solution (1M, 1 mL) and incubated with shaking for 30 min to release the protein captured by the nanocomposites. Recycling from the imidazole solution by a magnet, Fe_3O_4@$NiSiO_3$ nanocomposites were washed with PBS buffer and sonication for 30 min and further incubated with PBS solution for reuse.

Purification of His-Tagged Proteins in *E. coli*. The gene for expression of His-tagged enhanced green fluorescent protein (EGFP) was cloned in PET-28a vector to generate plasmid pet28a-EGFP, which was transformed into *E. coli* BL21 (DE3) competent cells. A single transformed colony was inoculated into 5 mL of Luria–Bertani (LB, 10 g L^{-1} tryptone, 5 g L^{-1} yeast extract, and 10 g L^{-1} NaCl) medium containing 50 μg·mL^{-1} kanamycin and grown overnight at 37 °C. The overnight culture was inoculated 1:100 into fresh LB medium containing 50 μg mL^{-1} kanamycin and grown at 37 °C until the optical density at 600 nm (OD_{600}) reached 0.8. Then, isopropyl-β-D-thiogalactopyranoside (IPTG) was added to a final concentration of 0.8 mM, and the culture was induced for 3–5 h at 37 °C. The bacteria were harvested by centrifugation (6000g, 10 min), and resuspended in phosphate buffered saline (pH 7.4) with 1.0 mM PMSF. After disrupting the cell by sonication on ice, the cell lysate was centrifuged (9000 g, 15 min; 4 °C) to remove the crude precipitates. Then, the Fe_3O_4@$NiSiO_3$ nanocomposites were added the above lysate and incubated for 30 min at room temperature in table concentrator with slight shaking. Subsequently, the precipitates were collected by an assistant magnet and washed with the PBS solutions for several times to remove nonspecifically adsorbed lysates. At last, the precipitates were mixed with an imidazole solution (1 M, 20 mL) and incubated with shaking for 30 min to release His-tagged GFP from the Fe_3O_4@$NiSiO_3$ nanocomposites. The recovered His-tagged GFP was analyzed by SDS-PAGE.

In Vitro Cytotoxicity Study. In vitro cytotoxicity was measured using standard 3-(4,5-dimethylthialzol-2-yl)-2,5-diphenyltetrazolium bromide (MTT) assays. Briefly, Hep-G2 cells were seeded in a 96-well plate at approximately 1×10^4 cells per well and incubated for 12 h at 37 °C in 5% CO_2 to allow cells to attach. Then, serial concentrations of DMEM solutions of Fe_3O_4@$NiSiO_3$ (25, 50, 100, 150, 200, 250, and 300 μg mL^{-1}, diluted in DMEM and containing 10% FBS, 200 mL/well) were added to the wells of the treatment group, and DMEM containing 10% FBS (200 mL per well) to the negative control group, respectively. After 12 h coincubation at 37 °C under 5% CO_2, the MTT solution (20 mL, 5 mg mL^{-1}) was added to each well and further incubated for an additional 4 h at 37 °C under 5% CO_2. Subsequently, 10% sodium dodecyl sulfate (SDS, 150 mL per well) was added and the assay plate was allowed to stand at room temperature for 12 h. Finally, the optical density at 570 nm (absorption value) was measured by a BioTek Eon monochromator-based multifunction microplate reader.

Measurements and Characterizations. SEM was performed by using a HITACHI S-4800 microscope at an accelerating voltage of 5 kV. TEM observations were performed by a Philips CM200UT microscope at a typical accelerating voltage of 160 kV and element mapping was used by FEI TITAN Titan ChemiSTEM. XRD was carried out by means of a Rigaku D/max-2550pc instrument with monochromatized Cu Kα radiation and a scanning step of 0.02°. Materials surface areas, N_2 adsorption isotherms (77.3 K) and pore size distributions were measured using Micromeritics ASAP 2020 M surface area and porosity analyzer. The magnetic properties of samples were collected on a MPM-XL-5 superconducting quantum interference device (SQUID) magnetometer at room temperature. Fluorescence spectra were recorded with a JASCO FP-6500 spectrofluorometer.

RESULTS AND DISCUSSION

The oleate-capped Fe_3O_4 nanoparticles were fabricated by a thermal decomposition method in 1-octadecene solution.[39] As shown in Figure 1A, the Fe_3O_4 nanoparticles were monodispersed

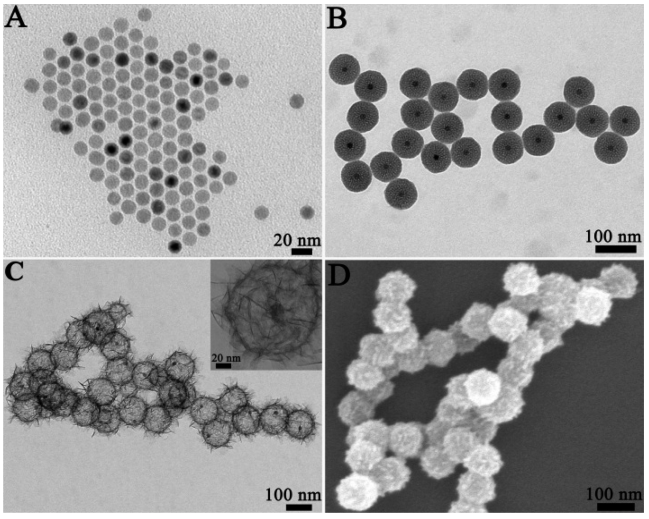

Figure 1. TEM images of (A) Fe_3O_4, (B) Fe_3O_4@SiO_2, (C) Fe_3O_4@$NiSiO_3$; (D) SEM image of Fe_3O_4@$NiSiO_3$.

and had a uniform size distribution with a size of about 15 nm. They could be dispersed excellently in nonpolar solvent such as hexane. The hydrophobic Fe_3O_4 nanoparticles were transferred from chloroform to aqueous solution by using CTAB and became water-dispersible nanoparticles. Subsequently, tetraethyl orthosilicate (TEOS) was added in weak basic condition (pH ~9) and the SiO_2 shell were formed on the surface of the Fe_3O_4 nanospheres via the sol–gel reaction. A single Fe_3O_4 core within SiO_2 shell was formed by hydrolysis of TEOS. Figure 1B demonstrated that the obtained Fe_3O_4@SiO_2 nanoparticles were also monodispersed and had a uniform size distribution with the spherical diameter of about 78 nm. Figure 1C displayed the TEM image of the Fe_3O_4@$NiSiO_3$ nanocomposites, demonstrating that the morphologies of the obtained products were spherical and well-dispersed. The size of the Fe_3O_4@$NiSiO_3$ nanocomposite was about 105 nm, and the surface of the nanocomposites is rough and presented needle-like structure. The as-prepared nanocomposites exhibited a typical yolk–shell nanostructure, and the most nickel silicate yolk shells encapsulate only one Fe_3O_4 nanoparticle. Figure 1C further indicated that the place of the Fe_3O_4 core in the hollow nickel silicate shell was random and usually not located in the center. The higher-magnification TEM image (inset of Figure 1C) showed that the nickel silicate shell presented hierarchically which was assembled by plenty of thin nanosheets. SEM image in Figure 1D further indicated that the morphology of the obtained nanomaterials also was near-spherical and the surfaces of the spherical particles were rough, which agreed well with the TEM observations.

The yolk–shell structure and the composition of the composite were ascertained by using element mapping of energy-dispersive X-ray (EDX) spectroscopy. In Figure 2A, STEM-HAADF (high-angle annular dark field) mode image demonstrated the successful yolk–shell nanostructures of Fe_3O_4@$NiSiO_3$ composites, which clearly presented a hierarchical thin shell and a core with the bright dots in the image. The distributions of Fe, Ni, Si, and O were presented in Figure 2. The core area clearly displayed the existence of Fe element (Figure 2C). The presence of nickel and silicon were strictly confined in the shell area (Figure 2D, E). The oxygen element distributed in both the core and the shell areas (Figure 2B). This result confirmed the yolk–shell structure of Fe_3O_4@$NiSiO_3$ composite. To test the stability of the yolk–shell nanostructures, we applied a 30 min sonication to treat Fe_3O_4@$NiSiO_3$ nanocomposites in aqueous solution. We found that the yolk–shell nanostructure remained well after the treatment (see Figure S1 in the Supporting Information). Even at a high temperature with 60 °C under intense sonication, the nanoparticles also kept the integrality with the yolk–shell nanostructure. Those experiments proved the excellent stability of Fe_3O_4@$NiSiO_3$ nanocomposites during the processes of the absorption and release of biomolecules.

The crystallographic structure of the product was further determined by XRD. Figure 3A showed the XRD patterns of Fe_3O_4, Fe_3O_4@SiO_2, and Fe_3O_4@$NiSiO_3$. Fe_3O_4 could be indexed as a face-cantered cubic structure (JCPDS 19–629).[5,6] The reflection characteristic of amorphous SiO_2 was appeared in the pattern of Fe_3O_4@SiO_2. The presences of diffraction peaks at 19.4, 26.7, 33.7, 53.2, and 60.4° in the pattern of Fe_3O_4@$NiSiO_3$ corresponded to the (100), (103), (110), (200), (210), (300) planes, respectively, of nickel silicate crystal (JCPDS 43–0664).[38] Figure 3B presented the FTIR spectra of Fe_3O_4, Fe_3O_4@SiO_2, and Fe_3O_4@$NiSiO_3$ nanocomposites. The absorption peak at 580 cm^{-1} corresponded to the Fe–O vibration related to the magnetite phase (cure a).[5] Compared

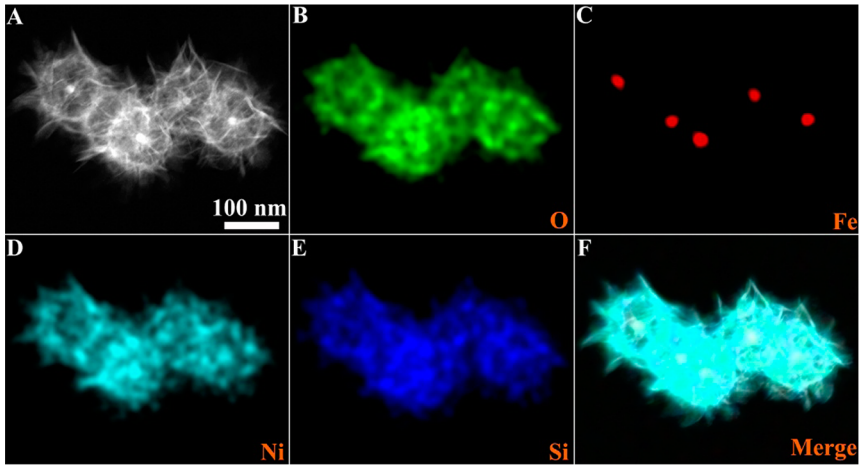

Figure 2. (A) STEM-HAADF image of Fe_3O_4@$NiSiO_3$ nanocomposites and element mapping images of Fe_3O_4@$NiSiO_3$ nanocomposites: (B) O element, (C) Fe element, (D) Ni element, (E) Si element, (F) merge.

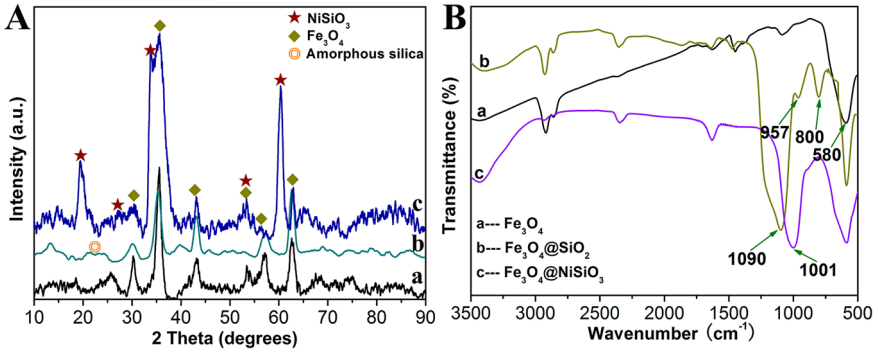

Figure 3. (A) XRD patterns of (a) Fe_3O_4, (b) Fe_3O_4@SiO_2, (c) Fe_3O_4@$NiSiO_3$; (B) FTIR spectra of (a) Fe_3O_4, (b) Fe_3O_4@SiO_2, (c) Fe_3O_4@$NiSiO_3$.

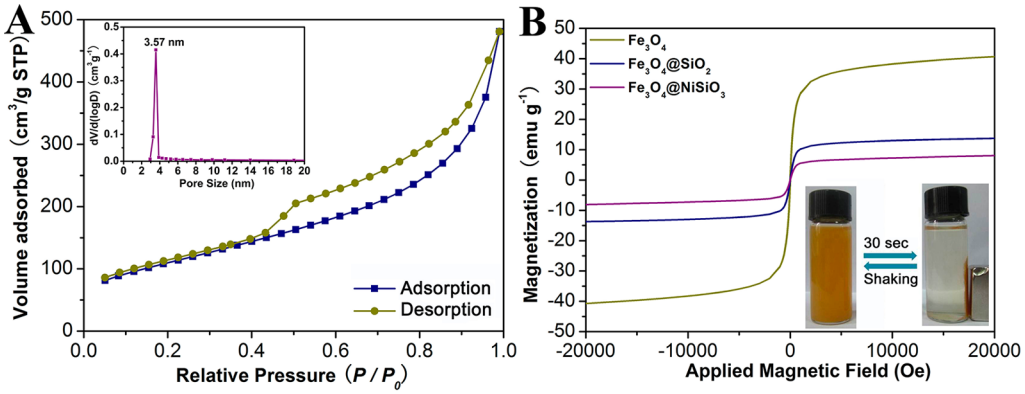

Figure 4. (A) N_2 sorption isotherms and pore size distribution (inset) of Fe_3O_4@$NiSiO_3$ nanocomposites. (B) Room-temperature (300 K) magnetic hysteresis loops of Fe_3O_4, Fe_3O_4@SiO_2, and Fe_3O_4@$NiSiO_3$, and photograph of magnetic separation and redispersion process of Fe_3O_4@$NiSiO_3$ nanocomposites in water solution.

with Fe_3O_4, the cure b presented an intense adsorption peak at 1090 cm^{-1} and two weak peaks at 957 and 800 cm^{-1}, which could be ascribed to the vibrations of Si−O−Si, Si−OH, and Si−O groups in the SiO_2 shell.[40] In cure c, two adsorption peaks at 957 and 800 cm^{-1} disappeared, and the peak at 1090 cm^{-1} was shifted to 1001 cm^{-1}, which might be ascribed to the formation of Si−O−Ni bonds.[37] Based on the combined TEM, EDS, XRD, and FTIR results, the yolk−shell nanocomposites with magnetic Fe_3O_4 cores and hierarchical $NiSiO_3$ shells have been successfully synthesized via such a facile and simple approach.

The N_2 adsorption and desorption analysis was then introduced to investigate the specific surface area and porosity of the yolk−shell structured Fe_3O_4@$NiSiO_3$ nanocomposites. The N_2 adsorption−desorption isotherms (Figure 4A) exhibited a typical IV-type isotherm, indicating the presence of mesoporous structure. The pore-size distribution plot confirmed that the nanocomposites have well-developed mesopores with a diameter of 3.57 nm. The special surface area and total pore volume were 396.3 $m^2\ g^{-1}$ and 0.74 $cm^3\ g^{-1}$, respectively, due to the mesoporous and hollow structures. Figure 4B shown that the magnetic hysteresis loops of Fe_3O_4, Fe_3O_4@SiO_2, and Fe_3O_4@$NiSiO_3$ at room temperature (T = 300 K) and the saturation magnetization values were 42.2, 14.2, and 8.8 emu g^{-1}, respectively. Compared with Fe_3O_4, the magnetization of Fe_3O_4@SiO_2 and Fe_3O_4@$NiSiO_3$ was decreased by the shell-involved mass increasing. The Fe_3O_4@$NiSiO_3$ nanocomposites could be dispersed readily in water via vigorous shaking or sonication to form a deep-yellow-colored suspension. The nanocomposites could also be fast aggregated by an external magnetic field from their homogeneous dispersion. After removing of the magnetic field, the redispersion of the nanocomposites occurred quickly with a slight shaking (inset of Figure 4B). These results show that the yolk−shell nanocomposites would provide combined advantages for biomolecule enrichments.

Using multifunctional nanomaterials for simple and effective separation and purification of proteins is very important for many of the advancements made in nanotechnology. Selecting appropriate techniques is the key step for efficient separation and purification of proteins. One of the typical techniques of protein purified is by IMAC which based on the coordination bonds between Ni^{2+} toward histidine via the formation and disassociation to realize the separation and purified of the proteins. In the present work, the as-prepared Fe_3O_4@$NiSiO_3$ nanocomposites could be directly used to selectively bind and magnetically separate the His-tagged proteins. As illustrated in Scheme 2, a mixture solution of His-tagged GFP and untagged GFP were used. The as-prepared Fe_3O_4@$NiSiO_3$ was added in mixture solution of proteins and incubated with shaking for 30 min. Subsequently, the precipitates were isolated from the mixture solution by using a magnet, and then added in an imidazole solution and incubated with shaking. His-tagged GFP could be released from Fe_3O_4@$NiSiO_3$ nanocomposites via a replacement by excess imidazole. The recovered Fe_3O_4@$NiSiO_3$ nanocomposites were washed with a PBS solution and could be used in a repeatable manner for the selective protein separation.

Figure 5A presented the photographs of the separation process after different reaction times. After incubating with the

dx.doi.org/10.1021/am505041a | ACS Appl. Mater. Interfaces 2014, 6, 19092−19099

Scheme 2. Schematic Representation of the Magnetically Recyclable Protein Separation Process Using Yolk−shell Fe_3O_4@$NiSiO_3$ Nanocomposites

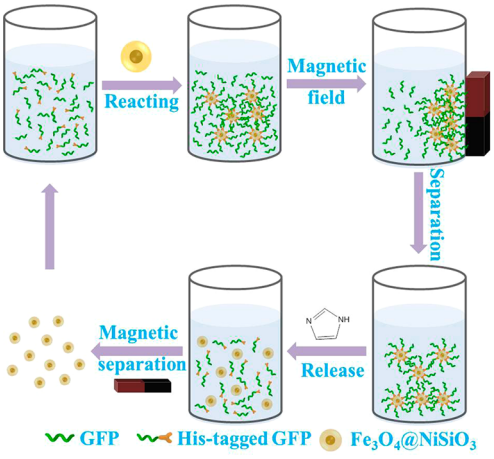

Fe_3O_4@$NiSiO_3$ nanocomposites for 30 min, the color of the mixture solution gradually changed from green to colorless, which indicated the fast and successful adsorption of His-tagged GFP by the nanocomposites. His-tagged GFP protein was presented green colored under UV excitation (inset of Figure 5B). The solution became colorless after incubation with Fe_3O_4@$NiSiO_3$ nanocomposites and the separation of Fe_3O_4@$NiSiO_3$/His-tagged GFP from the mixture solution by using a magnet. Finally, the color of the solution turned green again after released His-tagged GFP from Fe_3O_4@$NiSiO_3$ in imidazole solution. However, the color of the control group had no obvious change under UV excitation before and after reacting with normal GFP (inset of Figure 5C). To quantify the protein separation efficacy, we presented the fluorescent spectra of protein in Figure 5B, C. The spectrum before the addition of Fe_3O_4@$NiSiO_3$ showed the maximum intensity at 510 nm. After incubation with Fe_3O_4@$NiSiO_3$, the intensity of the fluorescent spectrum decreased with 99.9% due to the His-tagged GFP bound to Fe_3O_4@$NiSiO_3$, whereas only a 14.5% decrease in the intensity was observed for the GFP without His-tagged. It followed that in comparison with the untagged protein, Fe_3O_4@$NiSiO_3$ nanocomposites could exhibit superior binding properties to the His-tagged protein. After the release of His-tagged GFP in imidazole solution, the intensity of the

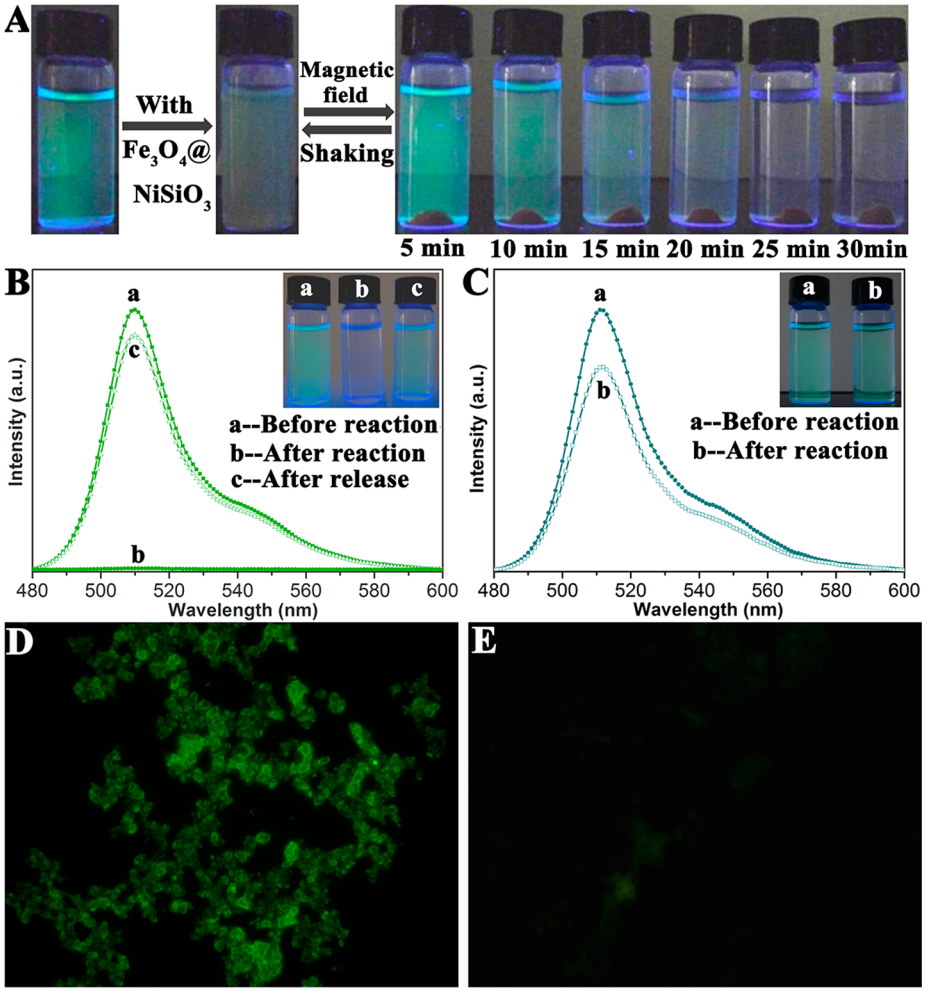

Figure 5. (A) Photographs of separation of His-tagged GFP by Fe_3O_4@$NiSiO_3$ nanocomposites after different times. (B) Fluorescent spectra of His-tagged GFP showing the change of emission intensity of the solution: (a) before and (b) after reaction with Fe_3O_4@$NiSiO_3$ nanocomposites for 30 min, (c) released His-tagged GFP in imidazole solution. (C) Fluorescent spectra of GFP showing the change of emission intensity of the solution: (a) before and (b) after reaction with Fe_3O_4@$NiSiO_3$ nanocomposites for 30 min. Fluorescence microscopic images of (D) His-tagged GFP/Fe_3O_4@$NiSiO_3$ nanocomposites and (E) GFP/Fe_3O_4−$NiSiO_3$ nanocomposites.

dx.doi.org/10.1021/am505041a | ACS Appl. Mater. Interfaces 2014, 6, 19092−19099

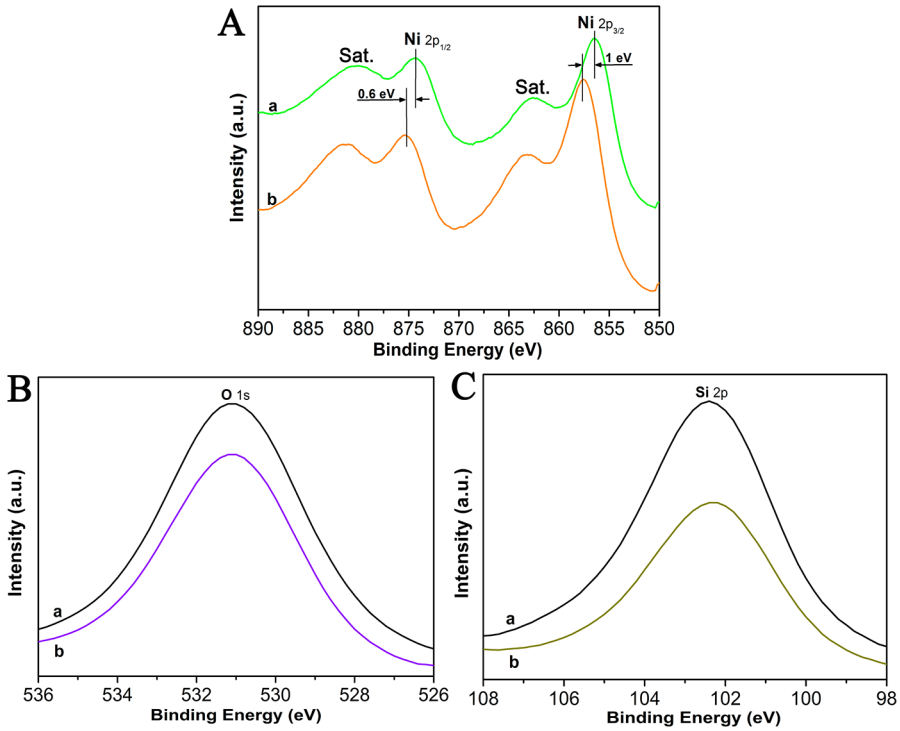

Figure 6. XPS spectra in the (A) Ni 2p, (B) O 1s, and (C) Si 2p regions for the Fe_3O_4@$NiSiO_3$ before and after reaction with His-tagged GFP: (a) Fe_3O_4@$NiSiO_3$, and (b) Fe_3O_4@$NiSiO_3$/His-GFP.

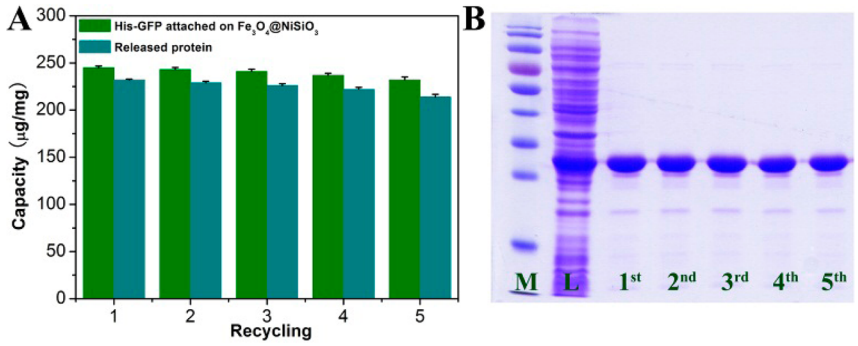

Figure 7. (A) Magnetic separation and recycling of Fe_3O_4@$NiSiO_3$ nanocomposites in the separation of His-tagged GFP. (B) SDS-PAGE analysis of cell lysate containing His-tagged GFP (L) and proteins released from the Fe_3O_4@$NiSiO_3$ nanocomposites by reused up to five times. Lane M is a molecular weight marker.

fluorescent spectrum showed that 91% of His-tagged GFP was successfully separated from the original protein solution. The fluorescence microscopic image of His-tagged GFP/Fe_3O_4@$NiSiO_3$ nanocomposites after magnetic separation showed strong green fluorescence (Figure 5D), whereas extremely weak green emission was observed for GFP/Fe_3O_4@$NiSiO_3$ nanocomposites (Figure 5E). This phenomenon confirmed the selective affinity of His-tagged protein to the surface of Fe_3O_4@$NiSiO_3$ nanocomposites. Another His-tagged protein of IgG (labeled by Cy3) was selected to repeat the above experiments and the result demonstrated that the as-synthesized Fe_3O_4@$NiSiO_3$ nanocomposites also had a high efficiency for selective affinity and separation of His-tagged IgG protein (see Figure S2 in the Supporting Information). It followed the universality of the Fe_3O_4@$NiSiO_3$ nanocomposites for His-tagged proteins selective separation.

To further comprehend the interaction between Fe_3O_4@$NiSiO_3$ nanocomposites and His-tagged protein, we obtained a fine-scanned XPS of Ni for Fe_3O_4@$NiSiO_3$ nanocomposites before and after the reactions with His-tagged GFP (Figure 6A). For Fe_3O_4@$NiSiO_3$ nanocomposites, the measured binding energies of Ni $2p_{1/2}$ and Ni $2p_{3/2}$ were 875.4 and 856.6 eV, respectively (Figure 6A, curve a), which were in agreement with those observed in $NiSiO_3$.[37] The appearance of satellite peaks (labeled "Sat.", Figure 6A) implied the presence of a high-spin divalent state of Ni^{2+} in the samples.[41,42] However, a significant shift has been observed in the XPS spectrum of Ni which after reaction with His-tagged GFP (Figure 6A, curve b). The binding energies of Ni $2p_{1/2}$ and Ni $2p_{3/2}$ shift to 874.8 and 855.6 eV, respectively, suggested an interaction between Ni^{2+} in the Fe_3O_4@$NiSiO_3$ and the His-tagged protein.[43] However, the XPS spectra of O and Si did not present any significant changes (Figure 6B, C). It followed that only Ni^{2+} contributed to the specific interaction with the His-tagged proteins. This conclusion was also validated by a parallel experiment using Fe_3O_4@$NiSiO_3$ and imidazole. There were slight changes of the

binding energies of Ni $2p_{1/2}$ and Ni $2p_{3/2}$ in Fe_3O_4@$NiSiO_3$ after its reaction with imidazole, and the XPS spectra of O and Si did not show any changes (see Figure S3 in the Supporting Information). This result indicated that only Ni^{2+} had a specific interaction with imidazole, which agreed with the phenomenon between the Fe_3O_4@$NiSiO_3$ nanocomposites and His-tagged proteins.

Because of the excellent magnetic responsivity, the magnetic separation and recycling of Fe_3O_4@$NiSiO_3$ nanocomposites was examined. In Figure 7A, after five times of the magnetic separation and release of His-GFP, the binding capacities of the Fe_3O_4@$NiSiO_3$ nanocomposites had no significant decrease. This excellent behavior might be attributed to the high surface area of the yolk−shell hierarchical structure of Fe_3O_4@$NiSiO_3$ nanocomposites, which provided more docking sites for His-tagged proteins and magnetic cores allowing easy manipulation. In comparison with the previously reported nano systems of Fe_3O_4−NTA−Ni^{2+},[22−24] Fe_2O_3/SiO_2@NiO,[27,28] Ni^{2+}-decorated superparamagnetic particles,[24] the yolk−shell Fe_3O_4@$NiSiO_3$ nanocomposites with high specific surface area had more efficiency for selective affinity and separation of His-tagged proteins. Even after five cycles of reuse, the absorption level of the yolk−shell Fe_3O_4@$NiSiO_3$ nanocomposites for His-tagged GFP protein still reached at a high level of 220 μg/mg. To test the actual practical applications of the nanocomposites for the separation of His-tagged proteins, we induced the expression of His-GFP in an *E. coli*. Then, the Fe_3O_4@$NiSiO_3$ nanocomposites were incubated in the cell lysate of *E. coli* and separated by use of a magnetic field. We reused Fe_3O_4@$NiSiO_3$ nanocomposites up to five times through the magnetic separation and subsequent release of the captured protein and employed SDS-PAGE gel electrophoresis to check the released proteins. The analysis showed that the His-GFP were well-separated by the nanocomposites up to five times (Figure 7B), and the affinity and specificity of Fe_3O_4@$NiSiO_3$ remained unaffected. It followed the good selectivity and recyclability of the material for the separation of His-tagged proteins in the *E. coli* cell lysate. A cell viability experiment was also proceeded to evaluate the cytotoxicity of Fe_3O_4@$NiSiO_3$ nanocomposites. The assessment showed that the Fe_3O_4@$NiSiO_3$ nanocomposites had no obvious toxicity for Hep-G2 cells (see Figure S4 in the Supporting Information). Therefore, the yolk−shell nanostructured Fe_3O_4@$NiSiO_3$ nanocomposites would have potential applications in biomedicine, particularly in targeted-drug delivery and biosensors.

CONCLUSIONS

We have fabricated the yolk−shell nanostructured Fe_3O_4@$NiSiO_3$ by a facile sol−gel and hydrothermal method. The outer shell of nickel silicate could provide for a selective adsorption of His-tagged protein from the mixed-protein solutions, and the magnetic Fe_3O_4 core allows the nanocomposites to be isolated from the solution by using a magnet. The selectivity and recyclability of Fe_3O_4@$NiSiO_3$ nanocomposites for the His-tagged protein were maintained well after several cycles, which would facilitate the biomedical applications of nanomaterials in targeted-drug delivery and biosensors.

ASSOCIATED CONTENT

Supporting Information

This material is available free of charge via the Internet at http://pubs.acs.org.

AUTHOR INFORMATION

Corresponding Author

*E-mail: rtang@zju.edu.cn. Fax: (+) 86-571-87953736.

Notes

The authors declare no competing financial interest.

ACKNOWLEDGMENTS

We thank Qiaohong He, Fang Chen, and Jieru Wang for their assistances in characterizations. This work was supported by the National Natural Science Foundation of China (91127003) and the Fundamental Research Funds for the Central Universities.

REFERENCES

(1) Wang, H.; Chen, L.; Feng, Y.; Chen, H. Exploiting Core-Shell Synergy for Nanosynthesis and Mechanistic Investigation. *Acc. Chem. Res.* **2013**, *46*, 1636−1646.

(2) Hu, S. H.; Liao, B. J.; Chiang, C. S.; Chen, P. J.; Chen, I. W.; Chen, S. Y. Core-Shell Nanocapsules Stabilized by Single-Component Polymer and Nanoparticles for Magneto-Chemotherapy/Hyperthermia with Multiple Drugs. *Adv. Mater.* **2012**, *24*, 3627−3632.

(3) Wei, S.; Wang, Q.; Zhu, J.; Sun, L.; Lin, H.; Guo, Z. Multifunctional Composite Core-Shell Nanoparticles. *Nanoscale* **2011**, *3*, 4474−4502.

(4) Reiss, P.; Protière, M.; Li, L. Core/Shell Semiconductor Nanocrystals. *Small* **2009**, *5*, 154−168.

(5) Wang, Y.; Shen, Y.; Xie, A.; Li, S.; Wang, X.; Cai, Y. A Simple Method To Construct Bifunctional Fe_3O_4/Au Hybrid Nanostructures and Tune Their Optical Properties in the Near-Infrared Region. *J. Phys. Chem. C* **2010**, *114*, 4297−4301.

(6) Wang, Y.; Li, S.; Xing, X.; Huang, F.; Shen, Y.; Xie, A.; Wang, X.; Zhang, J. Self-Assembled 3D Flowerlike Hierarchical Fe_3O_4@Bi_2O_3 Core-Shell Architectures and Their Enhanced Photocatalytic Activity under Visible Light. *Chem.—Eur. J.* **2011**, *17*, 4802−4808.

(7) Huang, X.; Guo, C.; Zuo, J.; Zheng, N.; Stucky, G. D. An Assembly Route to Inorganic Catalytic Nanoreactors Containing Sub-10-nm Gold Nanoparticles with Anti-Aggregation Properties. *Small* **2009**, *5*, 361−365.

(8) Lee, J.; Park, J. C.; Song, H. A Nanoreactor Framework of a Au@SiO_2 Yolk/Shell Structure for Catalytic Reduction of p-Nitrophenol. *Adv. Mater.* **2008**, *20*, 1523−1528.

(9) Tang, F.; Li, L.; Chen, D. Mesoporous Silica Nanoparticles: Synthesis, Biocompatibility and Drug Delivery. *Adv. Mater.* **2012**, *24*, 1504−1534.

(10) Zhao, Y.; Jiang, L. Hollow Micro/Nanomaterials with Multilevel Interior Structures. *Adv. Mater.* **2009**, *21*, 3621−3638.

(11) Ikeda, S.; Ishino, S.; Harada, T.; Okamoto, N.; Sakata, T.; Mori, H.; Kuwabata, S.; Torimoto, T.; Matsumura, M. Ligand-Free Platinum Nanoparticles Encapsulated in a Hollow Porous Carbon Shell as a Highly Active Heterogeneous Hydrogenation Catalyst. *Angew. Chem., Int. Ed.* **2006**, *118*, 7221−7224.

(12) Kim, S.; Yin, Y.; Alivisatos, A. P.; Somorjai, G. A.; Yates, J. T. IR Spectroscopic Observation of Molecular Transport through Pt@CoO Yolk-Shell Nanostructures. *J. Am. Chem. Soc.* **2007**, *129*, 9510−9513.

(13) Kuo, C.-H.; Tang, Y.; Chou, L.-Y.; Sneed, B. T.; Brodsky, C. N.; Zhao, Z.; Tsung, C.-K. Yolk-Shell Nanocrystal@ZIF-8 Nanostructures for Gas-Phase Heterogeneous Catalysis with Selectivity Control. *J. Am. Chem. Soc.* **2012**, *134*, 14345−14348.

(14) Sun, H.; Shen, X.; Yao, L.; Xing, S.; Wang, H.; Feng, Y.; Chen, H. Measuring the Unusually Slow Ionic Diffusion in Polyaniline via Study of Yolk-Shell Nanostructures. *J. Am. Chem. Soc.* **2012**, *134*, 11243−11250.

(15) Marinakos, S. M.; Novak, J. P.; Brousseau, L. C.; House, A. B.; Edeki, E. M.; Feldhaus, J. C.; Feldheim, D. L. Gold Particles as Templates for the Synthesis of Hollow Polymer Capsules. Control of Capsule Dimensions and Guest Encapsulation. *J. Am. Chem. Soc.* **1999**, *121*, 8518−8522.

(16) Jiang, P.; Bertone, J. F.; Colvin, V. L. A Lost-Wax Approach to Monodisperse Colloids and Their Crystals. *Science* **2001**, *291*, 453−457.
(17) Lou, X. W.; Yuan, C.; Rhoades, E.; Zhang, Q.; Archer, L. A. Encapsulation and Ostwald Ripening of Au and Au-Cl Complex Nanostructures in Silica Shells. *Adv. Funct. Mater.* **2006**, *16*, 1679−1684.
(18) Caruso, F.; Caruso, R. A.; Möhwald, H. Nanoengineering of Inorganic and Hybrid Hollow Spheres by Colloidal Templating. *Science* **1998**, *282*, 1111−1114.
(19) Jain, P.; Sun, L.; Dai, J.; Baker, G. L.; Bruening, M. L. High-Capacity Purification of His-tagged Proteins by Affinity Membranes Containing Functionalized Polymer Brushes. *Biomacromolecules* **2007**, *8*, 3102−3107.
(20) Clairbois, A. S.; Letourneur, D.; Muller, D.; Jozefonvicz, J. High-Performance Affinity Chromatography for the Purification of Heparin-Binding Proteins from Detergent-Solubilized Smooth Muscle Cell Membranes. *J. Chromatogr. B* **1998**, *706*, 55−62.
(21) Zou, H.; Luo, Q.; Zhou, D. Affinity Membrane Chromatography for the Analysis and Purification of Proteins. *J. Biochem. Biophys. Methods* **2001**, *49*, 199−240.
(22) Xu, C.; Xu, K.; Gu, H.; Zhong, X.; Guo, Z.; Zheng, R.; Zhang, X.; Xu, B. Nitrilotriacetic Acid-Modified Magnetic Nanoparticles as a General Agent to Bind Histidine-Tagged Proteins. *J. Am. Chem. Soc.* **2004**, *126*, 3392−3393.
(23) Xu, C.; Xu, K.; Gu, H.; Zheng, R.; Liu, H.; Zhang, X.; Guo, Z.; Xu, B. Dopamine as A Robust Anchor to Immobilize Functional Molecules on the Iron Oxide Shell of Magnetic Nanoparticles. *J. Am. Chem. Soc.* **2004**, *126*, 9938−9939.
(24) Liu, Z.; Li, M.; Li, Z.; Pu, F.; Ren, J.; Qu, X. Easy Access to Selective Binding and Recyclable Separation of Histidine-Tagged Proteins Using Ni^{2+}-Decorated Superparamagnetic Nanoparticles. *Nano Res.* **2012**, *5*, 450−459.
(25) Oh, B.-K.; Park, S.; Millstone, J. E.; Lee, S. W.; Lee, K.-B.; Mirkin, C. A. Separation of Tricomponent Protein Mixtures with Triblock Nanorods. *J. Am. Chem. Soc.* **2006**, *128*, 11825−11829.
(26) Lee, I. S.; Lee, N.; Park, J.; Kim, B. H.; Yi, Y.-W.; Kim, T.; Kim, T. K.; Lee, I. H.; Paik, S. R.; Hyeon, T. Ni/NiO Core/Shell Nanoparticles for Selective Binding and Magnetic Separation of Histidine-Tagged Proteins. *J. Am. Chem. Soc.* **2006**, *128*, 10658−10659.
(27) Kim, J.; Piao, Y.; Lee, N.; Park, Y. I.; Lee, I.-H.; Lee, J.-H.; Paik, S. R.; Hyeon, T. Magnetic Nanocomposite Spheres Decorated with NiO Nanoparticles for a Magnetically Recyclable Protein Separation System. *Adv. Mater.* **2010**, *22*, 57−60.
(28) Liu, Z.; Li, M.; Pu, F.; Ren, J.; Yang, X.; Qu, X. Hierarchical Magnetic Core-Shell Nanoarchitectures: Non-Linker Reagent Synthetic Route and Applications in a Biomolecule Separation System. *J. Mater. Chem.* **2012**, *22*, 2935−2942.
(29) Zheng, J.; Wu, B.-H.; Jiang, Z.-Y.; Kuang, Q.; Fang, X.-L.; Xie, Z.-X.; Huang, R.-B.; Zheng, L.-S. General and Facile Syntheses of Metal Silicate Porous Hollow Nanostructures. *Chem. Asian. J.* **2010**, *5*, 1439−1444.
(30) Fang, Q.; Xuan, S.; Jiang, W.; Gong, X. Yolk-like Micro/Nanoparticles with Superparamagnetic Iron Oxide Cores and Hierarchical Nickel Silicate Shells. *Adv. Funct. Mater.* **2011**, *21*, 1902−1909.
(31) Wang, Y.; Wang, G.; Wang, H.; Cai, W.; Zhang, L. One-Pot Synthesis of Nanotube-Based Hierarchical Copper Silicate Hollow Spheres. *Chem. Commun.* **2008**, 6555−6557.
(32) Wan, Y.; Zhao, D. On the Controllable Soft-Templating Approach to Mesoporous Silicates. *Chem. Rev.* **2007**, *107*, 2821−2860.
(33) Wang, Y.; Wang, G.; Wang, H.; Liang, C.; Cai, W.; Zhang, L. Chemical-Template Synthesis of Micro/Nanoscale Magnesium Silicate Hollow Spheres for Waste-Water Treatment. *Chem.—Eur. J.* **2010**, *16*, 3497−3503.
(34) Wang, X.; Zhuang, J.; Chen, J.; Zhou, K.; Li, Y. Thermally Stable Silicate Nanotubes. *Angew. Chem., Int. Ed.* **2004**, *43*, 2017−2020.
(35) Wu, J.; Zhu, Y.-J.; Cao, S.-W.; Chen, F. Hierachically Nanostructured Mesoporous Spheres of Calcium Silicate Hydrate: Surfactant-Free Sonochemical Synthesis and Drug-Delivery System with Ultrahigh Drug-Loading Capacity. *Adv. Mater.* **2010**, *22*, 749−753.
(36) Liu, C.; Monson, C. F.; Yang, T.; Pace, H.; Cremer, P. S. Protein Separation by Electrophoretic-Electroosmotic Focusing on Supported Lipid Bilayers. *Anal. Chem.* **2011**, *83*, 7876−7880.
(37) Wu, Y.; Chang, G.; Zhao, Y.; Zhang, Y. Preparation of Hollow Nickel Silicate Nanospheres for Separation of His-tagged Proteins. *Dalton Trans.* **2014**, *43*, 779−783.
(38) Liu, Z.; Li, M.; Yang, X.; Yin, M.; Ren, J.; Qu, X. The Use of Multifunctional Magnetic Mesoporous Core/Shell Heteronanostructures in a Biomolecule Separation System. *Biomaterials* **2011**, *32*, 4683−4690.
(39) Park, J.; An, K.; Hwang, Y.; Park, J.-G.; Noh, H.-J.; Kim, J.-Y.; Park, J.-H.; Hwang, N.-M.; Hyeon, T. Ultra-Large-Scale Syntheses of Monodisperse Nanocrystals. *Nat. Mater.* **2004**, *3*, 891−895.
(40) Sen, T.; Sebastianelli, A.; Bruce, I. J. Mesoporous Silica-Magnetite Nanocomposite: fabrication and Applications in Magnetic Bioseparations. *J. Am. Chem. Soc.* **2006**, *128*, 7130−7131.
(41) Huang, X.; Li, G.; Cao, B.; Wang, M.; Hao, C. Morphology Evolution and CL Property of Ni-Doped Zinc Oxide Nanostructures with Room-Temperature Ferromagnetism. *J. Phys. Chem. C* **2009**, *113*, 4381−4385.
(42) Liu, X. F.; Sun, Y.; Yu, R. H. Role of Oxygen Vacancies in Tuning Magnetic Properties of Co-doped SnO_2 Insulating Films. *J. Appl. Phys.* **2007**, *101*, 123907−123913.
(43) Shao, M.; Ning, F.; Zhao, J.; Wei, M.; Evans, D. G.; Duan, X. Preparation of Fe_3O_4@SiO_2@Layered Double Hydroxide Core-Shell Microspheres for Magnetic Separation of Proteins. *J. Am. Chem. Soc.* **2012**, *134*, 1071−1077.